Imaging a photodynamic therapy photosensitizer *in vivo* with a time-gated fluorescence tomography system

Weirong Mo
Daniel Rohrbach
Ulas Sunar

Imaging a photodynamic therapy photosensitizer *in vivo* with a time-gated fluorescence tomography system

Weirong Mo, Daniel Rohrbach, and Ulas Sunar
Roswell Park Cancer Institute, Department of Cell Stress Biology and PDT Center, Elm and Carlton Streets, Buffalo, New York, 14263

Abstract. We report the tomographic imaging of a photodynamic therapy (PDT) photosensitizer, 2-(1-hexyloxyethyl)-2-devinyl pyropheophorbide-a (HPPH) *in vivo* with time-domain fluorescence diffuse optical tomography (TD-FDOT). Simultaneous reconstruction of fluorescence yield and lifetime of HPPH was performed before and after PDT. The methodology was validated in phantom experiments, and depth-resolved *in vivo* imaging was achieved through simultaneous three-dimensional (3-D) mappings of fluorescence yield and lifetime contrasts. The tomographic images of a human head-and-neck xenograft in a mouse confirmed the preferential uptake and retention of HPPH by the tumor 24-h post-injection. HPPH-mediated PDT induced significant changes in fluorescence yield and lifetime. This pilot study demonstrates that TD-FDOT may be a good imaging modality for assessing photosensitizer distributions in deep tissue during PDT monitoring. © *2012 Society of Photo-Optical Instrumentation Engineers (SPIE).* [DOI: 10.1117/1.JBO.17.7.071306]

Keywords: fluorescence; diffusion; tomography; imaging system; image reconstruction; photodynamic therapy.

Paper 11602SS received Oct. 14, 2011; revised manuscript received Feb. 20, 2012; accepted for publication Mar. 5, 2012; published online May 16, 2012.

1 Introduction

Photodynamic therapy (PDT) is a clinically attractive treatment option for eradicating early-stage cancers.[1–3] With high tumor avidity, the chlorin-based compound 2-(1-hexyloxyethyl)-2-devinyl pyropheophorbide-a (HPPH) has been shown to be a potential photosenstizer for imaging and treatment.[4] Recent HPPH-oriented laboratory research and early-phase clinical studies at Roswell Park Cancer Institute (RPCI) have demonstrated that HPPH-mediated PDT is an effective treatment option for superficial cancers such as skin and head and neck lesions in the oral cavity.[4–8]

The efficacy of PDT is largely dependent on the spatial distribution and temporal changes of the photosensitizer.[9–11] Fluorescence properties of photosensitizers can be utilized to assess the photosensitizer content. Due to its simplicity, fluorescence spectroscopy has been employed in many preclinical and clinical studies (see reviews in Refs. 9 and 12). However, fluorescence spectroscopy is not well suited for quantifying spatial heterogeneities of optical properties, especially when deeper and thicker tissue is being investigated. In recent years, noninvasive near-infrared fluorescence diffuse optical tomography (FDOT) technologies emerged as viable approaches for imaging heterogeneities in deep tissue. For example, FDOT has been utilized as quantitative imaging for the localization of fluorophores in deeply seated tumors, as well as for therapy monitoring.[13–32]

Among FDOT modalities, the time-domain (TD) modality provides superior sensitivity over continuous-wave FDOT and frequency-domain FDOT for detecting weak fluorescence signals.[33–35] It can quantify absolute concentration and depth of a fluorophore by analyzing time-of-flight measurements.[36–41] In addition, TD-FDOT offers quantification of another imaging contrast: fluorescence lifetime.[14,42–48] As an intrinsic property of a fluorophore, the fluorescence lifetime is independent of fluorescence signal intensity, allowing time domain to be a robust technique for tumor demarcation.[35,49–53] Fluorescence lifetime may change in response to local molecular and cellular changes such as binding, polarity, pH value, and oxygenation status.[34,54,55] As such, changes in fluorophore lifetime can be potential noninvasive biomarkers for investigating and visualizing the local microvascular changes, photophysical processes, and photochemical reactions at molecular and cellular levels.[55–59] For example, microscopic TD imaging has been applied for studying photobleaching and lifetime dynamics of PDT photosensitizers in cells.[55,56,60,61]

In this paper, we report the application of TD-FDOT for 3-D reconstructions of the fluorescence yield and lifetime of the photosensitizer HPPH *in vivo* before and after PDT. We first describe a TD-FDOT system, which employs an ultra-short pulse laser, gated imaging, and time-delay techniques. We demonstrate the performance of the imaging system in resolving the fluorescence yield and lifetime of HPPH with phantom experiments. Then we show *in vivo* mouse imaging results. Further, we quantify the changes in these parameters due to PDT. Our imaging results show that the HPPH preferentially accumulated in the tumor, which allowed accurate localization of the tumor. In addition we show depth-resolved photobleaching and lifetime changes due to HPPH-mediated PDT. This study demonstrates the utility of the TD-FDOT system for monitoring PDT with fluorescence yield and lifetime contrasts.

2 Methods

2.1 Experimental TD-FDOT System

Figure 1 shows the schematic of our experimental TD-FDOT system. Planar transmission geometry was adopted to achieve

Address all correspondence to: Ulas Sunar, Roswell Park Cancer Institute, Department of Cell Stress Biology and PDT Center, Elm and Carlton Streets, Buffalo, New York, 14263; Tel.: +1 7168453311; Fax: +1 7168458920; E-mail: ulas.sunar@roswellpark.org
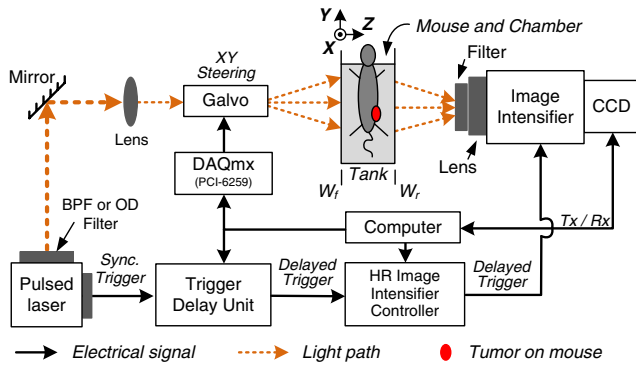
Fig. 1 Schematic of time-domain fluorescence diffuse optical tomography (TD-FDOT) system.

large-area tissue sampling with the combination of a galvanometer scanner and a lens coupled charge-coupled device (CCD) camera.[15,16,42] A 660 nm pulsed laser (BHLP-660, Becker & Hickl GmbH) was used as the light source to match HPPH's absorption peak at 665 nm.[5] The laser has a pulse repetition rate of 50 MHz. The average optical power was set to ~0.5 mW, and the full-width-at-half-maximum (FWHM) of the laser pulse was ~120 ps. The spectrum of the collimated laser beam was first corrected with a bandpass filter (BPF) in front of the laser, and then the laser beam was focused on the front wall of the imaging chamber (W_f in Fig. 1). The imaging chamber was sandwiched between two pieces of transparent, antireflection-coated glass, allowing an imaging volume of 80 mm × 80 mm × 18 mm. Homogenous optical matching fluid, prepared by mixing India ink, Intralipid suspension, and water, was poured into the tank to serve as the homogeneous image background for phantom and mice experiments. The emission signals from the rear wall (W_r in Fig. 1) sequentially passed through an optical filter, a collimation lens set (AF NIKKOR 50 mm f/1.4D, Nikon), and a high-gain image intensifier (PicoStar HR-12, LaVision) and was captured by a highly sensitive CCD camera (12 bit, Imager QE, LaVision). The high-gain image intensifier worked in a time-gated, or a "comb" mode, as described previously.[42] Briefly, each laser pulse (pulse rate = 50 MHz) synchronously produced a trigger signal, which served as a timing reference. This trigger opened a high-rate image intensifier (HRI) gate after a fixed time delays. Time delays can be set by a delay unit, and gate widths can be set by HRI. The intensifier boosts the signal originated from the object. The CCD camera collected the boosted optical signal and streams data into personal computer. The CCD camera exposure length determines the number of laser pulses that are integrated. As the pulsed laser had a repetition rate of 50 MHz, $5 × 10^7$ images could be accumulated if the CCD acquisition time was 1 s. As the trigger signals were delayed incrementally, the combination of image intensifier and CCD camera can record a sequence of images, which reflects the time-resolved photon intensity. An ultra-sharp, narrow bandpass filter (FF01-720/13-25, Semrock) in front of the image intensifier rejected undesired excitation photons. The incident laser beam was steered in an XY raster pattern by a high-quality programmable galvanometer scanner (ProSeries-10, Cambridge Technology). The entire experimental system was automated under computer control through a data acquisition module (NI-DAQmx, PCI-6259, National Instruments) and a custom LabVIEW (Version 8.5, National Instruments) program.

2.2 Data Acquisition

In order to acquire the time-resolved signals, the "comb" mode of the image intensifier was utilized. The gate width $\Delta\tau_{gate}$ was set to be 0.8 ns. The delay of the temporal acquisition, $\tau_{delay} = N \cdot \Delta\tau_{delay}$, $N = [1 \ldots N_d]$ was set to be $\tau_{delay} = [0, 0.8, 1.6, \ldots, 12]$ ns, where the incremental step $\Delta\tau_{delay} = 0.8$ ns and N_d is the number of delay steps. The bias voltage of the image intensifier V_{bias} (configurable in $[200 \ldots 850]$ V) was fixed at 670 V and the exposure time of the CCD, τ_{exp} was optimized to avoid signal saturations. These system settings are similar to previous work[42,62,63] and were optimized empirically with considerations of CCD's dynamic range, gain of the image intensifier, dark noise, HPPH dose and lifetime, and the data-acquisition time. In addition, the images acquired by the CCD camera binned to 128 × 128 pixels to increase the signal-to-noise ratio.

For each imaging experiment, three types of data sets were acquired: intrinsic excitation, fluorescence emission, and leakage. The data set of intrinsic laser excitation φ_{ex}, which characterizes the system response in the presence of the imaging objects, was acquired by mounting a neutral-density filter (OD2) in front of the image intensifier. The data set of fluorescence emission φ_{em} was acquired in a similar way, but by replacing the OD2 filter with a 720 nm bandpass fluorescence filter. The data set of leakage signal φ_{lk}, which accounted for the bleeding-through of excitation light through the fluorescence filter, was acquired in a similar way as fluorescence emission, but with no fluorescence object in the imaging chamber.[16,42,64,65] The exposure time τ_{exp} was 400 ms during excitation, emission, and leakage measurements. Figure 2 shows an example of a time-resolved excitation and emission data from a HPPH phantom experiment. The leakage signal was negligible (mean ± standard deviation of φ_{lk} was less than 2% of mean ± deviation of φ_{em}, data not shown) under these experimental settings and optical properties.

2.3 Image Reconstruction

The quantification of fluorescence yield and lifetime was based on the normalized Born approximation.[13,15,17,64] By making use of self-calibrated data that divide the fluorescence measurements with corresponding excitation measurements, the normalized Born ratio works with analytical or numerical forward solvers and offers significant experimental advantages as it is independent of source strengths, detector gains, coupling efficiency to tissue. These advantages significantly simplify the image reconstruction.[16,17,64,66] Such image reconstruction method was recently reported to resolve 50 ps lifetime changes with a similar instrumentation approach.[42] The acquired
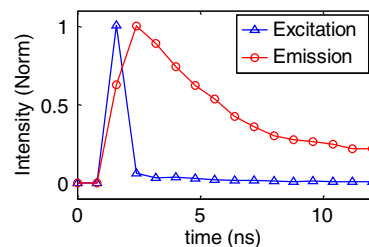

Fig. 2 Temporal profiles (normalized) obtained from HPPH experiment. (Red circle line): Fluorescence emission and (blue triangle line): Laser excitations.

time-resolved data were first converted into frequency domain. The real and imaginary information were extracted for resolving the fluorescence yield and lifetime simultaneously. Any harmonic frequencies ranging from base frequency f_{base} through maximum frequency $f_{\max} = N \cdot f_{\text{base}}$ can be utilized for image reconstruction, where integer N is the order of harmonics or the total time-delay steps.[42,45] For example, in the settings of HPPH experiments, 16 time-resolved images were acquired sequentially for a given time-step size of 0.8 ns. The information at fundamental frequency is thus, $f_{\text{base}} = [1/16 \text{ samples}/(0.8 \text{ ns/sample})] = 78.125$ Mhz and $f_{\max} = 16 \cdot f_{\text{base}} = 1.25$ GHz. For the results reported here, we used the fundamental frequency f_{base} for the image reconstruction. A MATLAB (R2009a, The MathWorks, Inc.) program was constructed to solve the discrete linear equation $\mathbf{\Phi}_{nB} = \mathbf{W} \cdot \mathbf{X}$, where

$$
\begin{aligned}
&\mathbf{\Phi}_{nB}[\mathbf{r}_{s(i)}, \mathbf{r}_{d(j)}, \omega] \\
&= \frac{\mathbf{\Phi}_{\text{em}}[\mathbf{r}_{s(i)}, \mathbf{r}_{d(j)}, \omega, \lambda_{\text{em}}] - \mathbf{\Phi}_{\text{lk}}[\mathbf{r}_{s(i)}, \mathbf{r}_{d(j)}, \omega, \lambda_{\text{ex}}]}{\mathbf{\Phi}_{\text{ex}}[\mathbf{r}_{s(i)}, \mathbf{r}_{d(j)}, \omega, \lambda_{\text{ex}}]},
\end{aligned} \quad (1)
$$

$$
\begin{aligned}
\mathbf{W}_{(i,j:k)} &= -S_0 \\
&\cdot \frac{\mathbf{G}_{sv}[\mathbf{r}_{s(i)}, \mathbf{r}_{v(k)}, \omega, \lambda_{\text{ex}}] \cdot \mathbf{G}_{vd}[\mathbf{r}_{v(k)}, \mathbf{r}_{d(j)}, \omega, \lambda_{\text{em}}]}{\mathbf{G}_{sd}[\mathbf{r}_{s(i)}, \mathbf{r}_{d(j)}, \omega, \lambda_{\text{ex}}]},
\end{aligned} \quad (2)
$$

$$
\mathbf{X}_k = \frac{\boldsymbol{\eta}_k \cdot \mu_a^{\text{em}}}{1 - i\omega \boldsymbol{\tau}_k}. \quad (3)
$$

Here $\mathbf{\Phi}_{nB}[\mathbf{r}_{s(i)}, \mathbf{r}_{d(j)}, \omega]$ is the normalized Born ratio of emission photon density to excitation photon density. The weight matrix $\mathbf{W}_{(i,j:k)}$ accounts for the perturbation of fluorescence heterogeneities at voxel $v(k)$ in response to the excitation at source position $\mathbf{r}_{s(i)}$ and the emission at the detector position $\mathbf{r}_{d(j)}$. $\mathbf{\Phi}_{\text{em}}[\mathbf{r}_{s(i)}, \mathbf{r}_{d(j)}, \omega]$ and $\mathbf{\Phi}_{\text{ex}}[\mathbf{r}_{s(i)}, \mathbf{r}_{d(j)}, \omega]$ are temporal point-spread functions (TPSF) of emission $\varphi_{\text{em}}[r_{s(i)}, r_{d(j)}]$ and excitation $\varphi_{\text{ex}}[r_{s(i)}, r_{d(j)}]$ in Fourier domain, respectively. λ_{em} and λ_{ex} are excitation wavelength and the emission wavelength, respectively. $\omega = 2\pi f_{\text{base}}$ is the fundamental angular frequency, which can be determined by the temporal sampling interval of the experiment. $\mathbf{G}$ is a two-point Green's function in frequency domain,[42,45] with an altered form in order to account for the slab boundary conditions,[67] S_0 is a calibration factor depending on the geometry and optical properties.[17] The unknown volumetric variable $\mathbf{X}_k$, which encompasses spatial variations of fluorescence yield $\boldsymbol{\eta}_k$ and lifetime $\boldsymbol{\tau}_k$, can be resolved by inverting the linear equation $\mathbf{\Phi}_{nB} = \mathbf{W} \cdot \mathbf{X}$. As a straightforward solution to this linear equation, in which complex numbers involved, terms of $\mathbf{\Phi}_{nB}$, $\mathbf{W}$, and $\mathbf{X}$ are decomposed and rewritten as

$$
\begin{bmatrix} \text{Re}(\mathbf{\Phi}_{nB}) \\ \text{Im}(\mathbf{\Phi}_{nB}) \end{bmatrix} = \begin{bmatrix} \text{Re}(\mathbf{W}) & -\text{Im}(\mathbf{W}) \\ \text{Im}(\mathbf{W}) & \text{Re}(\mathbf{W}) \end{bmatrix} \cdot \begin{bmatrix} \text{Re}(\mathbf{X}) \\ \text{Im}(\mathbf{X}) \end{bmatrix},
$$

where $\text{Re}(\cdot)$ and $\text{Im}(\cdot)$ stands for real and imaginary parts of the corresponding quantities, respectively. In this study, the algebraic reconstruction technique (ART) was used to iteratively resolve $\mathbf{X}_k$ and reconstruct images for both phantom and mouse data.[68] The 3-D mappings of fluorescence yield and lifetime can be achieved simultaneously by rearranging the volumetric vector

$$
\mathbf{X}_k \text{ by } \boldsymbol{\tau}_k = \frac{\text{Im}(\mathbf{X}_k)}{\omega \cdot \text{Re}(\mathbf{X}_k)} \quad \text{and}
$$

$$
\boldsymbol{\eta}_k = \text{Re}(\mathbf{X}_k) + \omega \cdot \boldsymbol{\tau}_k \cdot \text{Im}(\mathbf{X}_k).
$$

2.4 Phantom and In Vivo Imaging

The laser scanning pattern was set to be an 8×8 grid, giving a total of 64 source positions (blue "+" in Fig. 3). The laser beam had a diameter of ~0.3 mm when focused on the imaging tank and was assumed to be a point source. The point-to-point separation was 3 mm, giving a total scanning area of ~24 mm $\times$ 24 mm. For mouse imaging, this scanning area could cover the tumor with some peripheral tissue. On the detection plane ($Z = 18$ mm), we chose 64 pixels, which had identical X and Y positions as 64 source positions (red "circle" in Fig. 2). Each pixel, having a spatial area of ~0.4 mm $\times$ 0.4 mm, was assumed as an infinitesimal point detector. In total 4096 source-to-detector measurements were selected. At each laser source position, 15 consecutive temporal images ($N_d = 15$) were acquired with an increasing temporal interval of $\Delta\tau_{\text{delay}} = 0.8$ ns, giving a temporal length of 12 ns.

Phantom experiments were conducted prior to the mouse experiments. The optical matching fluid with absorption coefficient $\mu_a = 0.4$ cm^{-1} and reduced scattering coefficient $\mu_s' = 10.0$ cm^{-1} was filled into the imaging tank to mimic the optical properties of healthy mouse tissue. The absorption and reduced scattering coefficients were assumed to be similar at excitation and emission wavelengths. Hence these two parameters were substituted into the normalized Born ratio as fixed values. A transparent plastic tube (diameter = 5 mm), containing HPPH fluorophore (concentration = 0.5 μM) in identical matching fluid, was inserted into the tank vertically at the position $(X, Z) \approx (-4.0, 9.0)$ mm to mimic the tumor heterogeneity.

In order to characterize the accuracy of the image reconstruction, especially the fluorophore's lifetime, we conducted another phantom experiment using a well-known fluorescence compound, Atto655 (93711, Sigma-Aldrich). We chose Atto655 because it has similar excitation and emission peaks ($\lambda_{\text{ex}} = 665$ nm, $\lambda_{\text{em}} = 690$ nm) and the same order of magnitude lifetime (1.9 ns in water), which allowed using similar experimental settings. The tube containing Atto655 (concentration = 0.5 μM) in optical matching fluid was placed vertically on the position $(X, Z) \approx (4.0, 9.0)$ mm.
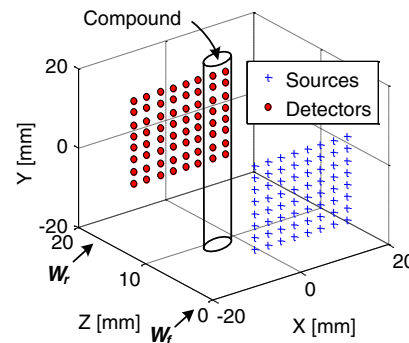

Fig. 3 Illustration of transmission geometry. Blue "+": laser scanning positions on the source plane (W_f, $Z = 0$ mm). Red "•": detector positions on the detection plane (W_r, $Z = 18$ mm). The 64 detectors have identical X-Y positions as 64 source positions.
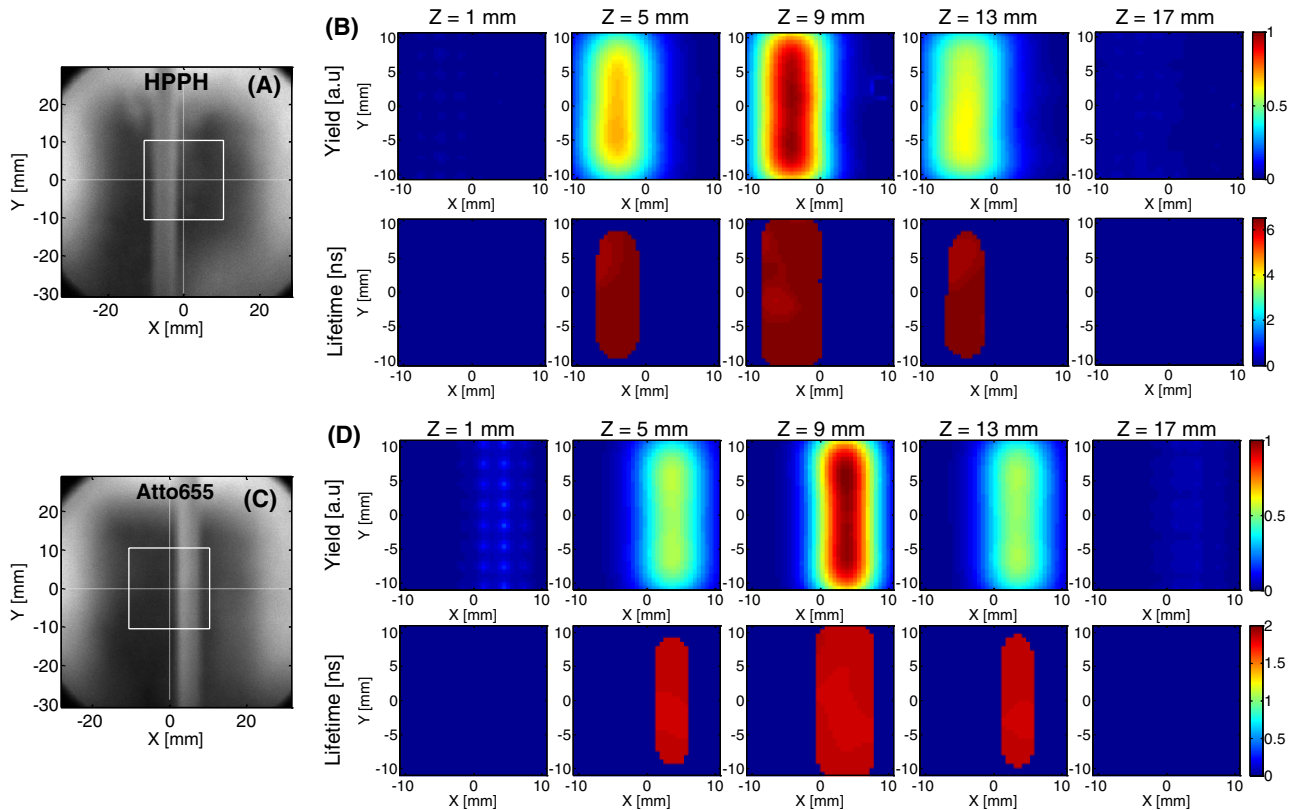
Fig. 4 (a) Picture of phantom tube containing HPPH. White square shows the region of laser scanning and image reconstruction. (b) Reconstructed images of fluorescence yield (top, unit: a.u) and lifetime (bottom, unit: ns) of HPPH at 5 different depths $Z = (1, 5, 9, 13, 17)$ mm. (c) Picture of phantom tube containing Atto655. White square shows the region of laser scanning and image reconstruction. (d) Reconstructed images of fluorescence yield (top, unit: a.u) and lifetime (bottom, unit: ns) of Atto655 at five difference depths $Z = (1, 5, 9, 13, 17)$ mm.

The *in vivo* mouse imaging and PDT treatments in this study were performed in compliance with Roswell Park Cancer Institute Animal Study Committees' requirements. A male severe combined immunodeficiency (SCID) mouse (12 weeks old, weight 30 grams) was inoculated subcutaneously with human head and neck tumor tissue obtained from a patient during an ongoing clinical trial.[7] The tumor was planted on the right lateral flank of the mouse and grew up to a diameter of approximately 10 mm (Fig. 4). The photosensitizer HPPH (3 μmol/kg) was injected intravenously via tail vein 24-h before the imaging experiment and PDT treatment. To minimize motion artifacts during scanning, the mouse was anesthetized with ketamine (100 mg/kg), xylazine (10 mg/kg), and acepromazine (3 mg/kg). The anesthetized mouse was secured in a holder to minimize motion and discomfort. The holder with the mouse was submerged into the matching fluid-filled tank. The optical properties of the matching fluid were identical to those of the matching fluid made for phantom experiments. The temperature of the matching fluid was kept around 35°C to prevent loss of body heat. The mouse's head was above the fluid for normal breathing and the mouse's eyes were lubricated with tear gel to avoid drying.

During the PDT laser treatment, the mouse remained in the imaging chamber while the optical matching fluid was removed. The tumor area plus a small peripheral margin (16 mm diameter spot size) was irradiated with 75 mW/cm^2 of 665 nm light from an Argon pumped dye laser. The treatment took 10 min for a total dose of 45 Joules/cm^2, and a single imaging scan took ~12 min. During the entire imaging and treatment period, the mouse was kept anesthetized.

3 Results and Discussion

3.1 Phantom Imaging

Figure 4(a) and 4(c) show the photographic pictures of HPPH and Atto655 phantom tubes and imaging area (white squares), while Fig. 4(b) and 4(d) show how the corresponding image reconstruction results in terms of fluorescence yield (top, unit: a.u) and lifetime (bottom, unit: ns), respectively. For tomographic image reconstruction, the imaging chamber (slab thickness, total depth = 18 mm) was evenly divided into five non-overlapping slices, spanning from depth $Z_1 = 1.0$ mm through depth $Z_5 = 17.0$ mm with a depth increment of 4 mm. X and Y coronal images were reconstructed at these five depths. After image reconstruction, for the lifetime quantification we demarcated the object size by including any voxel with yield values of at least 30% of the maximum yield.[45] Based on the thresholded lifetime images, the mean lifetime within the HPPH target area is found to be (6.39 ± 0.11) ns (mean $\pm$ standard deviation), which is within the range of published results.[69] From the HPPH images, the position of the tube axis was found to be $(X, Z) = (-4.0 \pm 0.5, 9.0 \pm 0.5)$ mm, which agrees with the real center position $(X, Z) = (-4.0 \pm 0.5, 9.0 \pm 0.5)$ mm. Moreover, the mean lifetime of Atto655 was found to be (1.86 ± 0.16) ns, which closely agrees with the standard value of 1.9 ns. Although we did not fully
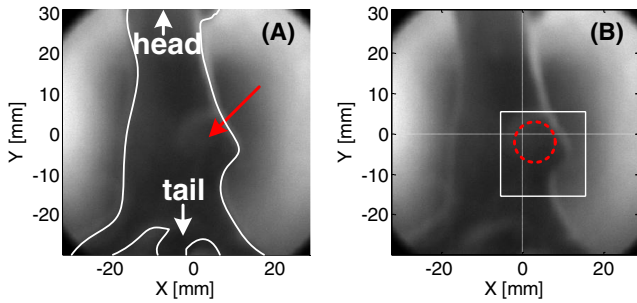
Fig. 5 (a) Picture of mouse outlined by white curves, and tumor position pointed by red arrow; (b) region of interested outlined by the white square will be reconstructed. Red circle shows the tumor area.

characterized the accuracy of our system in estimating lifetimes, a recent study by Nothdurft et al.[42] reported a 50 ps lifetime sensitivity using a similar system and reconstruction strategy.

3.2 In Vivo Mouse Imaging

The mouse imaging was reconstructed in a similar way as the phantom images. Figure 5(a) shows the picture of the mouse outlined by white curves and tumor position pointed by red arrow. Figure 5(b) shows the scanned and imaged tumor area and surrounding peripheral normal tissues. The area in the white square shows the laser scanning and image reconstruction areas. The tumor area, indicated by the red circle, was located approximately in the top-left quadrant. The same mouse was
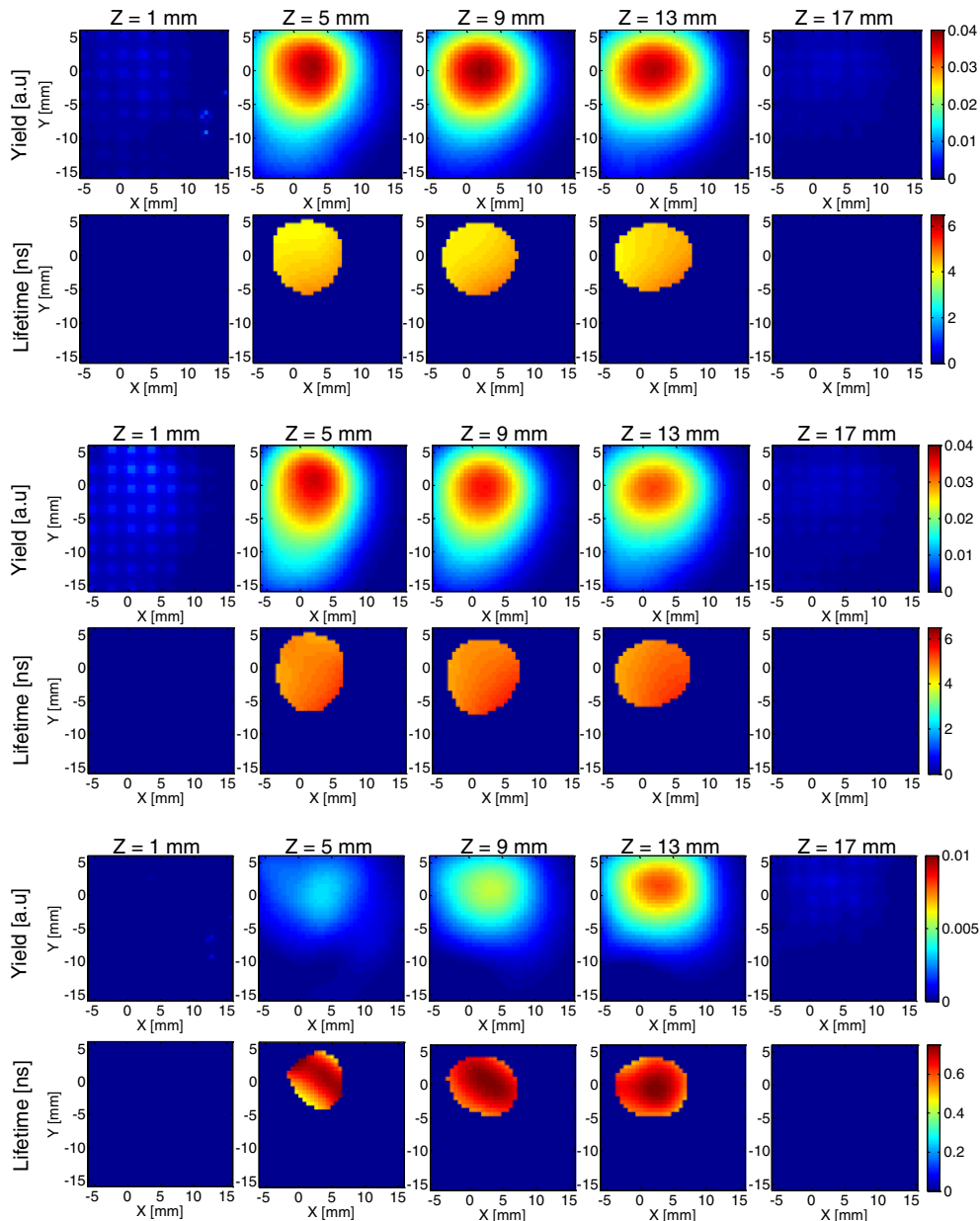

Fig. 6 Image reconstruction results of mouse tumor and peripheral areas. The top two rows show fluorescence yield and lifetime tomography before PDT. The middle two rows show corresponding results after PDT. The bottom two rows show the difference by subtracting "after" (2nd two rows) from "before" (1st two rows).
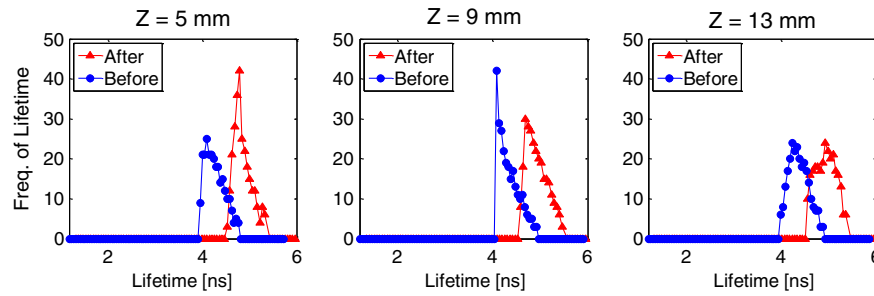
Fig. 7 Histograms of fluorescence lifetime at pre-PDT (blue-dot-line) and post-PDT (red-triangle-line). Y-axis is frequency (Freq.); x-axis is lifetime.

imaged twice, i.e., before PDT and after PDT, respectively. The reconstructed images are shown in Fig. 6 in a coronal perspective. From top to bottom, the first two rows show fluorescence yield [arbitrary units (a.u.)] and lifetime (ns) of HPPH before PDT irradiation. The middle two rows show the same quantities after PDT irradiation, and the last two rows show the differences of fluorescence yield and lifetime by subtracting the pre-PDT results from the post-PDT results. Lifetime images were thresholded by 30% of corresponding fluorescence yield images as before. Images at five different depths are shown from left to right with increasing depth order ($Z = [1, 5, 9, 13, 17]$ mm).

According to the reconstructed images, the position of tumor can be found at $(X, Y) = (2.0 \pm 1.0, 0.5 \pm 1.0)$ mm, which closely matches the real tumor position centered on $(X, Y) = (2.1 \pm 1.0, 1.0 \pm 1.0)$ mm. The high-intensity areas in the yield images show the HPPH was preferentially accumulated and retained by the tumor compared to surrounding normal tissues. Quantitative investigations of images show that HPPH was not completely photobleached during the 10-min laser irradiation. The relative change of fluorescence yield decreased from 0.04 (a.u.) to 0.034 (a.u.) at middle depth ($Z = 9$ mm), resulting in ~15% photobleaching.

The photobleaching was found to be depth-dependent due to the propagation of the PDT irradiation photons. For example, fluorescence yield photobleaching was higher (~20%) close to the detector plane ($Z = 13$ mm) where PDT treatment light was administered. Fluence rate (and photobleaching) is highest close to the laser irradiation plane and decreases as the photons of treatment light propagate through tissue. Figure 6 shows the *in vivo* peak photobleaching varied from ~20% (close to PDT illumination, $Z = 13$ mm) to 8% ($Z = 5$ mm, further than PDT light). These results verify that the TD-FDOT system can quantify changes in photosensitizer distributions at different depths.

At the PDT Center in our institute, usual treatment parameters of 75 mW/cm^2 of fluence rate, 30 min of total treatment time, and 135 Joules/cm^2 of total light dose are being used as an effective treatment. Thus due to time constraints, the dose given in our study was three times less than the usual dose. It is hard to compare the photobleaching amount with previous work since photobleaching is strongly dependent on available oxygen, vascular parameters such as blood flow and photosensizer distribution in the tumor. This human head and neck xenograft model is recently developed in our institute from extracted patient tumor tissue, and it can be very different than other tumor models. It is a more realistic representation of large head and neck patient tumor masses with high interstitial pressure, low oxygen partial pressure, and less vasculature.[70] Less vasculature with low blood flow may result in low level of accumulated photosensitizer dose. Low oxygenation

may result in inefficient photobleaching.[71] Moreover, photosensitizer distribution can be very different due to working mechanisms of the photosensitizer and tumor tissue types. Furthermore, one-to-one comparison to previous work requires imaging (preferably concurrently) a similar tissue volume. We are probing relatively deeper tissue volumes compared with typical superficial tissue being treated by PDT. In the near future experiments, we will image statistically significant number of animals and have opportunity to compare our *in vivo* results with the photosensitizer concentration obtained from excised tissues.

Figure 7 shows the pre-PDT (blue lines) and post-PDT (red lines) histograms of the reconstructed images of HPPH lifetime, which clearly reveal that the HPPH lifetime increased after PDT. The mean lifetime increased from approximately $[4.3 \pm 0.2]$ ns to $[5.0 \pm 0.2]$ ns, resulting in a ~16% of increase at the middle slice ($Z = 9$ mm). As much as ~700 ps change in lifetime is expected to be due to PDT-induced physiological changes such as changes in oxygenation (see Sud et al.)[57] and changes in the microenvironment of HPPH, such as changes in pH (see Scully et al.[55] and Sud et al.).[57] Lifetime increase is related to oxygenation decrease, which is highly possible since oxygen is being consumed during PDT. PDT can induce early blood flow increase (see Becker et al.),[72] and interstitial fluid pressure decrease, resulting in a decrease in tumor acidity and increase in pH, which is related to lifetime increase.[57] Thus our results indicate that lifetime changes can potentially be employed for PDT monitoring.

It should be pointed out that although the image reconstruction was performed at a single frequency in this work, the Fourier-transformed time domain data has multifrequency information. The image reconstruction is expected to improve by using multifrequencies instead of a single frequency due to more information content [as long as high signal-to-noise ratio (SNR) is kept during the analysis]. For example, multifrequency data can allow extracting background optical properties more accurately and provide *a priori* information for more accurate reconstructions of fluorescence properties.[73] Thus time-domain techniques have advantages over single-frequency-domain methods. However, if single-frequency data is going to be used, frequency-domain methods can be more advantageous in *in vivo* studies since they can provide simpler and cheaper instruments and higher SNR.

4 Conclusion

In this work, we report the application of time-domain fluorescence diffuse optical tomography to image the PDT induced changes in fluorescence yield and lifetime *in vivo*. The image reconstruction results verified that the tumor-avid compound HPPH accumulated preferentially in the tumor 24-h post injection.

The *in vivo* experiments showed the fluorescence yield of HPPH decreased and lifetime increased as a result of PDT. Our results highlight the potential that TD-FDOT can provide physiological and molecular level markers (such as fluorescence yield and lifetime) for monitoring PDT in preclinical and clinical settings.

Acknowledgments

References

1. M. A. MacCormack, "Photodynamic therapy in dermatology: an update on applications and outcomes," *Semin. Cutan. Med. Surg.* **27**(1), 52–62 (2008).
2. T. J. Dougherty, "An update on photodynamic therapy applications," *J. Clin. Laser Med. Surg.* **20**(1), 3–7 (2002).
3. A. Juzeniene, Q. Peng, and J. Moan, "Milestones in the development of photodynamic therapy and fluorescence diagnosis," *Photochem. Photobiol. Sci.* **6**(12), 1234–1245 (2007).
4. H. R. Nava et al., "Photodynamic therapy (PDT) using HPPH for the treatment of precancerous lesions associated with barrett's esophagus," *Laser. Surg. Med.* **43**(7), 705–712 (2011).
5. R. K. Pandey et al., "Nature: a rich source for developing multifunctional agents. Tumor-imaging and photodynamic therapy," *Laser. Surg. Med.* **38**(5), 445–467 (2006).
6. S. K. Pandey et al., "Multimodality agents for tumor imaging (PET, fluorescence) and photodynamic therapy. A possible 'see and treat' approach," *J. Med. Chem.* **48**(20), 6286–6295 (2005).
7. U. Sunar et al., "Monitoring photobleaching and hemodynamic responses to HPPH-mediated photodynamic therapy of head and neck cancer: a case report," *Opt. Express* **18**(14), 14969–14978 (2010).
8. X. Zheng et al., "Conjugation of 2-(1'-hexyloxyethyl)-2-devinylpyropheophorbide-a (HPPH) to carbohydrates changes its subcellular distribution and enhances photodynamic activity in vivo," *J. Med. Chem.* **52**(14), 4306–4318 (2009).
9. B. C. Wilson, M. S. Patterson, and L. Lilge, "Implicit and explicit dosimetry in photodynamic therapy: a new paradigm," *Laser. Med. Sci.* **12**(3), 182–199 (1997).
10. I. Georgakoudi and T. H. Foster, "Singlet oxygen- versus nonsinglet oxygen-mediated mechanisms of sensitizer photobleaching and their effects on photodynamic dosimetry," *Photochem. Photobiol.* **67**(6), 612–625 (1998).
11. Q. Peng et al., "Selective distribution of porphyrins in skin thick basal cell carcinoma after topical application of methyl 5-aminolevulinate," *J. Photochem. Photobiol. B* **62**(3), 140–145 (2001).
12. S. Andersson-Engels et al., "In vivo fluorescence imaging for tissue diagnostics," *Phys. Med. Biol.* **42**(5), 815–824 (1997).
13. V. Ntziachristos, "Fluorescence molecular imaging," *Annu. Rev. Biomed. Eng.* **8**, 1–33 (2006).
14. X. D. Li et al., "Fluorescent diffuse photon density waves in homogeneous and heterogeneous turbid media: analytic solutions and applications," *Appl. Opt.* **35**(19), 3746–3758 (1996).
15. E. E. Graves et al., "A submillimeter resolution fluorescence molecular imaging system for small animal imaging," *Med. Phys.* **30**(5), 901–911 (2003).
16. S. Patwardhan et al., "Time-dependent whole-body fluorescence tomography of probe bio-distributions in mice," *Opt. Express* **13**(7), 2564–2577 (2005).
17. V. Ntziachristos and R. Weissleder, "Experimental three-dimensional fluorescence reconstruction of diffuse media by use of a normalized Born approximation," *Opt. Lett.* **26**(12), 893–895 (2001).
18. A. D. Klose and A. H. Hielscher, "Fluorescence tomography with simulated data based on the equation of radiative transfer," *Opt. Lett.* **28**(12), 1019–1021 (2003).
19. R. B. Schulz et al., "Comparison of noncontact and fiber-based fluorescence-mediated tomography," *Opt. Lett.* **31**(6), 769–771 (2006).
20. J. Lee and E. M. Sevick-Muraca, "Three-dimensional fluorescence enhanced optical tomography using referenced frequency-domain photon migration measurements at emission and excitation wavelengths," *J. Opt. Soc. Am. A* **19**(4), 759–771 (2002).
21. X. Montet et al., "Tomographic fluorescence imaging of tumor vascular volume in mice," *Radiology* **242**(3), 751–758 (2007).
22. A. B. Milstein et al., "Fluorescence optical diffusion tomography," *Appl. Opt.* **42**(16), 3081–3094 (2003).
23. V. Ntziachristos et al., "Looking and listening to light: the evolution of whole-body photonic imaging," *Nat. Biotechnol.* **23**(3), 313–320 (2005).
24. D. Kepshire et al., "Fluorescence tomography characterization for sub-surface imaging with protoporphyrin IX," *Opt. Express* **16**(12), 8581–8593 (2008).
25. D. S. Kepshire et al., "Imaging of glioma tumor with endogenous fluorescence tomography," *J. Biomed. Opt.* **14**(3), 030501 (2009).
26. N. C. Biswal et al., "Fluorescence imaging of vascular endothelial growth factor in tumors for mice embedded in a turbid medium," *J. Biomed. Opt.* **15**(1), 016012 (2010).
27. J. Axelsson, J. Swartling, and S. Andersson-Engels, "*In vivo* photosensitizer tomography inside the human prostate," *Opt. Lett.* **34**(3), 232–234 (2009).
28. A. Corlu et al., "Three-dimensional in vivo fluorescence diffuse optical tomography of breast cancer in humans," *Opt. Express* **15**(11), 6696–6716 (2007).
29. Y. Lin et al., "Quantitative fluorescence tomography with functional and structural a priori information," *Appl. Opt.* **48**(7), 1328–1336 (2009).
30. V. Venugopal et al., "Full-field time-resolved fluorescence tomography of small animals," *Opt. Lett.* **35**(19), 3189–3191 (2010).
31. S. C. Davis et al., "Magnetic resonance-coupled fluorescence tomography scanner for molecular imaging of tissue," *Rev. Sci. Instrum.* **79**(6), 064302 (2008).
32. S. C. Davis et al., "MRI-coupled fluorescence tomography quantifies EGFR activity in brain tumors," *Acad. Radiol.* **17**(3), 271–276 (2010).
33. W. Becker, *Advanced Time-Correlated Single Photon Counting Techniques*, (Springer, Berlin (2005).
34. J. R. Lacowicz, *Principles of Fluorescence Spectroscopy* (Springer, Berlin 1999).
35. R. Cubeddu et al., "Time-resolved fluorescence imaging in biology and medicine," *J. Phys. D* **35**, R61–R76 (2002).
36. D. Hall et al., "Simple time-domain optical method for estimating the depth and concentration of a fluorescent inclusion in a turbid medium," *Opt. Lett.* **29**(19), 2258–2260 (2004).
37. S. H. Han and D. J. Hall, "Estimating the depth and lifetime of a fluorescent inclusion in a turbid medium using a simple time-domain optical method," *Opt. Lett.* **33**(9), 1035–1037 (2008).
38. D. J. Hall et al., "In vivo simultaneous monitoring of two fluorophores with lifetime contrast using a full-field time domain system," *Appl. Opt.* **48**(10), D74–78 (2009).
39. A. Laidevant et al., "Analytical method for localizing a fluorescent inclusion in a turbid medium," *Appl. Opt.* **46**(11), 2131–2137 (2007).
40. S. Lam, F. Lesage, and X. Intes, "Time domain fluorescent diffuse optical tomography: Analytical expressions," *Opt. Express* **13**(7), 2263–2275 (2005).
41. J. Boutet et al., "Bimodal ultrasound and fluorescence approach for prostate cancer diagnosis," *J. Biomed. Opt.* **14**(6), 064001 (2009).
42. R. E. Nothdurft et al., "In vivo fluorescence lifetime tomography," *J. Biomed. Opt.* **14**(6), 024004 (2009).
43. A. T. Kumar et al., "Fluorescence-lifetime-based tomography for turbid media," *Opt. Lett.* **30**(24), 3347–3349 (2005).
44. A. T. Kumar et al., "A time domain fluorescence tomography system for small animal imaging," *IEEE Trans. Med. Imag.* **27**(8), 1152–1163 (2008).
45. M. A. O'Leary et al., "Fluorescence lifetime imaging in turbid media," *Opt. Lett.* **21**(2), 158–160 (1996).
46. A. Godavarty, E. M. Sevick-Muraca, and M. J. Eppstein, "Three-dimensional fluorescence lifetime tomography," *Med. Phys.* **32**(4), 992–1000 (2005).
47. F. Gao et al., "A linear, featured-data scheme for image reconstruction in time-domain fluorescence molecular tomography," *Opt. Express* **14**(16), 7109–7124 (2006).

48. J. Chen, V. Venugopal, and X. Intes, "Monte Carlo based method for fluorescence tomographic imaging with lifetime multiplexing using time gates," *Biomed. Opt. Express* **2**(4), 871–886 (2011).

49. R. Cubeddu et al., "Tumor detection in mice by measurement of fluorescence decay time matrices," *Opt. Lett.* **20**(24), 2553–2555 (1995).

50. R. Cubeddu et al., "Use of time-gated fluorescence imaging for diagnosis in biomedicine," *J. Photochem. Photobiol. B* **12**(1), 109–113 (1992).

51. R. Cubeddu et al., "Time-gated fluorescence imaging for the diagnosis of tumors in a murine model," *Photochem. Photobiol.* **57**(3), 480–485 (1993).

52. I. Munro et al., "Toward the clinical application of time-domain fluorescence lifetime imaging," *J. Biomed. Opt.* **10**(5), 051403 (2005).

53. S. Bloch et al., "Whole-body fluorescence lifetime imaging of a tumor-targeted near-infrared molecular probe in mice," *J. Biomed. Opt.* **10**(5), 054003 (2005).

54. M. Y. Berezin et al., "Ratiometric analysis of fluorescence lifetime for probing binding sites in albumin with near-infrared fluorescent molecular probes," *Photochem. Photobiol.* **83**(6), 1371–1378 (2007).

55. A. D. Scully et al., "Application of fluorescence lifetime imaging microscopy to the investigation of intracellular PDT mechanisms," *Bioimaging* **5**(1), 9–18 (1997).

56. J. A. Russell et al., "Characterization of fluorescence lifetime of Photofrin and delta-aminolevulinic acid induced protoporphyrin IX in living cells using single- and two-photon excitation," *IEEE J. Sel. Top. Quantum. Electron.* **14**(1), 158–166 (2008).

57. D. Sud et al., "Time-resolved optical imaging provides a molecular snapshot of altered metabolic function in living human cancer cell models," *Opt. Express* **14**(10), 4412–4426 (2006).

58. J. Siegel et al., "Studying biological tissue with fluorescence lifetime imaging: microscopy, endoscopy, and complex decay profiles," *Appl. Opt.* **42**(16), 2995–3004 (2003).

59. D. Elson et al., "Time-domain fluorescence lifetime imaging applied to biological tissue," *Photochem. Photobiol. Sci.* **3**(8), 795–801 (2004).

60. M. Kress et al., "Time-resolved microspectrofluorometry and fluorescence lifetime imaging of photosensitizers using picosecond pulsed diode lasers in laser scanning microscopes," *J. Biomed. Opt.* **8**(1), 26–32 (2003).

61. J. P. Connelly et al., "Time-resolved fluorescence imaging of photosensitiser distributions in mammalian cells using a picosecond laser line-scanning microscope," *J. Photochem. Photobiol. A* **142**(2–3), 169–175 (2001).

62. A. T. Kumar et al., "Time resolved fluorescence tomography of turbid media based on lifetime contrast," *Opt. Express* **14**(25), 12255–12270 (2006).

63. V. Y. Soloviev et al., "Fluorescence lifetime imaging by using time-gated data acquisition," *Appl. Opt.* **46**(3), 7384–7391 (2007).

64. A. Soubret, J. Ripoll, and V. Ntziachristos, "Accuracy of fluorescent tomography in the presence of heterogeneities: study of the normalized Born ratio," *IEEE Trans. Med. Imag.* **24**(10), 1377–1386 (2005).

65. V. Ntziachristos et al., "Planar fluorescence imaging using normalized data," *J. Biomed. Opt.* **10**(6), 064007 (2005).

66. V. Ntziachristos and R. Weissleder, "Charge-coupled-device based scanner for tomography of fluorescent near-infrared probes in turbid media," *Med. Phys.* **29**(5), 803–809 (2002).

67. M. S. Patterson, B. Chance, and B. C. Wilson, "Time resolved reflectance and transmittance for the noninvasive measurement of tissue optical properties," *Appl. Opt.* **28**(12), 2331–2336 (1989).

68. A. C. Kak and M. Slaney, *Principles of Computerized Tomographic Imaging*, IEEE Press, New York (1988).

69. O. Mermut et al., "Frequency domain, time-resolved and spectroscopic investigations of photosensitizers encapsulated in liposomal phantoms," *Proc. SPIE* **6632**, 66320P (2007).

70. M. Molls and P. Vaupel, *Blood Perfusion and Microenvironment of Human Tumors: Implications for Clinical Radiooncology*, (Springer, Berlin 2000).

71. B. C. Wilson and M. S. Patterson, "The physics, biophysics and technology of photodynamic therapy," *Phys. Med. Biol.* **53**(9), R61–R109 (2008).

72. T. L. Becker et al., "Monitoring blood flow responses during topical ALA-PDT," *Biomed. Opt. Express* **2**(1), 123–130 (2011).

73. S. V. Patwardhan and J. P. Culver, "Quantitative diffuse optical tomography for small animals using an ultrafast gated image intensifier," *J. Biomed. Opt.* **13**(1), 011009 (2008).